Ordered Structure in Mixtures of a Block Copolymer and Homopolymers. 1. Solubilization of Low Molecular Weight Homopolymers†

Hideaki Tanaka,‡ Hirokazu Hasegawa, and Takeji Hashimoto*

Department of Polymer Chemistry, Kyoto University, Kyoto 606, Japan

Received February 9, 1990; Revised Manuscript Received May 22, 1990

ABSTRACT: Microdomain structures of binary mixtures of poly(styrene-*b*-isoprene) diblock polymer (SI) and homopolystyrene (HS) and ternary mixtures of SI, HS, and homopolyisoprene (HI) were investigated as a function of volume fraction of SI (ϕ_b) in the mixtures for given molecular weights of HS (M_{HS}), HI (M_{HI}), and SI (M_b) and volume fraction of polystyrene (PS) block chain (f) in the block polymer SI at a strong segregation limit. The systems studied here have characteristics of $f = 0.45$, $M_{HS}/M_b = 0.068$, and $M_{HI}/M_b = 0.073$. The results indicated that (i) the homopolymers HS and HI are solubilized essentially uniformly in the corresponding microdomains, causing changes of the microdomain morphology with the change of total volume fraction of the constituent polymer, e.g., PS and the size of each microdomain, and that (ii) the long-range order of the microdomains is conserved down to a very low level of ϕ_b, with a ϕ_b as low as 0.10 being observed in this experiment.

I. Introduction

The morphology of microdomains formed by pure and simple block copolymers such as poly(styrene-*b*-isoprene) diblock polymers (SI) with only London-type dispersive interactions at a segregation limit has been well explored up to now.[1-6] Here we extend such studies to investigate the morphology of mixtures of SI with the corresponding homopolymers, e.g., homopolystyrene (HS) and homopolyisoprene (HI). The morphology is expected to be rich, though in a sense more complicated than the pure block polymer systems, since there is an interplay of two kinds of phase transitions:[7-9] (i) "microphase transition", i.e., the phase transition associated with liquid–liquid microphase separation and/or dissolution between block polystyrene (PS) and polyisoprene (PI) chains and (ii) "macrophase transition", i.e., the ordinary liquid–liquid phase separation and/or dissolution between different polymer species, i.e., between SI and HS or among SI, HS, and HI. The microphase transition generates the microdomain structure with a characteristic wavenumber $q_m \cong 2\pi/R_g$ in the thermal equilibrium where R_g is the gyration radius of SI. On the other hand, the macrophase transition generates the domains with $q_m \cong 0$, q_m being much smaller than $2\pi/R_g$, in the thermal equilibrium. It should be noted that some important theoretical[9] and experimental[10] studies were reported on the phase diagrams of such systems. Here we focus our research interest on the morphology of such mixtures with low molecular weight homopolymers in the strong segregation limit.

Figure 1 sketches three possible but extreme structures that may exist in binary mixtures of A–B diblock polymer and A homopolymer at the segregation limit. (a) "*Complete segregation*" between an A homopolymer phase and an A–B microdomain phase composed of A–B block polymer where A and B block chains segregate themselves into the respective microdomains, e.g., alternating lamellar microdomains of A and B block chains in the case when A and B blocks have about equal molecular volume and hence the volume fraction of A in A–B, f, is about $^1/_2$. Here a small amount of A homopolymer may be solubilized into A microdomains. (b) A homopolymers are solubilized into A microdomains, but A homopolymer chains are not

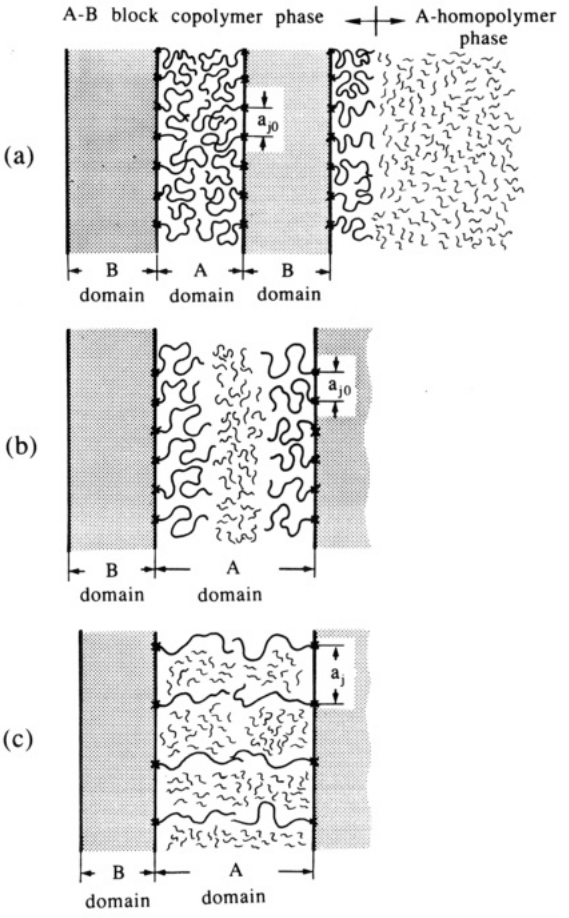

Figure 1. Schematic diagram showing the possible structures of the mixtures of A–B block polymer and A homopolymer: (a) the complete phase separation into A homopolymer phase and the phase containing the microdomains of the block polymer; (b) the uniform microdomain structure composed of A–B and A in which A homopolymer is locally solubilized in the middle of A microdomains; (c) the uniform microdomain structure composed of A–B and A in which A homopolymer is uniformly solubilized in A microdomains.

† Presented in part at the 34th Polymer Symposium of the Society of Polymer Science, Japan, Sept 1985. Tanaka, H.; Hasegawa, H.; Hashimoto, T. *Polym. Prepr., Jpn. Soc. Polym. Sci., Jpn.* **1985**, *34*, 2769.

‡ Present address: Mitsubishi Kasei Corp., Research Center, 1000 Kamoshida-cho, Midori-ku, Yokohama 227, Japan.

0024-9297/91/2224-0240$02.50/0

molecularly mixed with the A block chains and tend to be segregated in the central regions of A domains ("*localized solubilization*").[11,12,30] (c) A homopolymers are uniformly solubilized into A microdomains, and A homopolymer chains are mixed with A block chains on the molecular level ("*uniform solubilization*").

The extreme model (b) is physically identical with model (a) of the complete segregation in that (i) the conformations of A homopolymer chains, A block chains, and even B block chains, which are not shown in the schematic diagram, are unaffected by one another and that (ii) the average distance between the chemical junctions, a_{J0}, is unaffected at all by the localized solubilization. The localized solubilization expands the thickness of A lamellar microdomains but does hardly affect B domains, as it does not change a_{J0}.

On the other hand, the uniform solubilization generally invokes conformation changes of A homopolymer chains and A block chains. The chain conformations of A homopolymer and A block chains tend to be expanded along the direction normal to the interface. It also affects the conformation of B block chains and hence B microdomains, simply because it expands the average distance between the chemical junctions of SI from a_{J0} to a_J. The expansion of a_{J0} causes a contraction of the conformation of B block chains in the direction normal to the interface and hence a contraction of the thickness of B microdomains in order to maintain the constant density of B microdomains relevant to that of pure B homopolymer phase (incompressibility requirement).

As the amount of solubilized A homopolymers into A microdomains increases for the uniform solubilization model, the free-energy penalty caused by the conformational entropy loss increases. This penalty can be compensated by introducing a curvature in the interface, i.e., by changing the microdomain morphology from alternating lamellar microdomains with zero interface curvature to cylindrical microdomains and finally to spherical microdomains. These morphological transitions are expected to occur when the free-energy penalty caused by the interfacial curvature is outweighed by the free-energy penalty caused by the molecular conformations. In contrast to the uniform solubilization, one will not expect such morphological transitions in the case of the localized solubilization, simply because it does not involve a significant change in the molecular conformations of the A–B block polymer.

Figure 1 shows schematically only a few possible equilibrium structures. In general, there will be a numerous number of intermediate structures for the mixtures, which will be evolved during ordering processes at the phase transition. It will be an extremely fascinating research project to study the ordering processes and self-assembling patterns for the mixtures quenched into their miscibility gaps of various kinds,[8] e.g., (i) the gap where the mixtures are thermodynamically unstable both for the microphase and macrophase transitions and (ii) the gap where the mixtures are unstable for the microphase transition but stable or metastable for the macrophase transition, etc.

Nevertheless we impose here a restriction that M_{HS} and M_{HI} are much less than M_{SI}. This restriction suppresses the macrophase transition relative to the microphase transition,[8] so that the mixtures undergo only the microphase transition down to the very low level of ϕ_b, the volume fraction of SI diblock polymer in the binary mixtures (SI/HS mixtures) and in the ternary mixtures (SI/HS/HI mixtures). In a subsequent companion paper[12] we discuss the effect of increasing molecular weight of homopolymers on their solubilization behavior.

It is worth noting here that Kinning et al.[13] investigated morphology of the micelles or vesicles for binary mixtures of poly(styrene-*b*-butadiene) and polystyrene as a function of ϕ_b and M_{HS}. They studied morphology of the mixtures in the limit of small ϕ_b in which the block copolymer no longer forms the microdomains with a long-range spatial order. In contrast, in our study ϕ_b is greater than a critical value so that the block copolymer always forms the microdomains with the long-range order. Thus the two studies are quite complementary to each other and useful for a complete story.

Table I
Characterization of Specimens

specimens	specimen codes	$M_n \times 10^{-3}$	wt fraction of PS[c]	vol fraction of PS[d]	M_w/M_n[e]
SI	HY-8	31.6[a]	0.48	0.45	1.07
HS	S02	2.2[b]	1.0	1.0	1.10
HI	HI	2.3[b]	0.0	0.0	1.19

[a] Measured by membrane osmometry. [b] Measured by vapor pressure osmometry. [c] Measured by elemental analysis. [d] The mass density of PS and PI used are 1.052 and 0.925 g/cm^3. [e] Measured by size-exclusion chromatography.

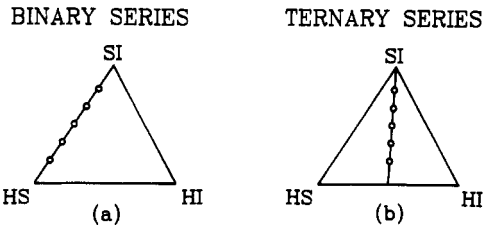

Figure 2. Triangular diagrams showing the compositions of (a) the binary mixtures of SI and HS and (b) the ternary mixtures of SI, HS, and HI.

II. Experimental Methods

1. **Specimens.** Block polymer SI and homopolymers HS and HI were prepared by living anionic polymerization with butyllithium as the initiator. Tetrahydrofuran (THF) was used as the reaction solvent at −78 °C for SI and HI and benzene at 30 °C for HS. SI was prepared by sequential living anionic polymerization. The polyisoprene (PI) homopolymer or block chains thus polymerized have the following microstructure as characterized by the IR method; 37–39%, 57–61%, and 1–4% for 1,2-, 3,4-, and 1,4-linkages, respectively.[14] Table I summarizes the characterization of the specimens. f is the volume fraction of PS in SI.

The film specimens of neat SI, SI/HS binary mixtures, and SI/HS/HI ternary mixtures with the compositions as shown by the open circles in the triangular diagrams of Figure 2 were prepared. The ternary mixtures were prepared along the isopleth line. The mixtures were prepared by dissolving the corresponding polymer mixtures in 10 wt % polymer solution with toluene as a neutrally good solvent for both PS and PI and by evaporating the solvent very slowly over 1 month at 30 °C. The film specimens were further dried in a vacuum oven until constant weights were attained. The ternary mixtures along the isopleth line were prepared by adding HS and HI to SI so as to maintain the total weight fraction of styrene monomer units equal to that of pure SI, i.e., 0.48. Thickness of the cast films was ca. 300 μm.

2. **Electron Microscopy.** The microdomain structures were examined by transmission electron microscopy. For this purpose small pieces of the as-cast films were first stained by osmium tetraoxide vapor and embedded in epoxy resin. Otherwise, the film specimens of the blends containing large volume fractions of the low molecular weight homopolymers were easily fractured into tiny pieces and were difficult to handle. The ultrathin sections of ca. 50 nm thick were obtained by using an LKB Model 4800 ultramicrotome with glass knives. The ultrathin

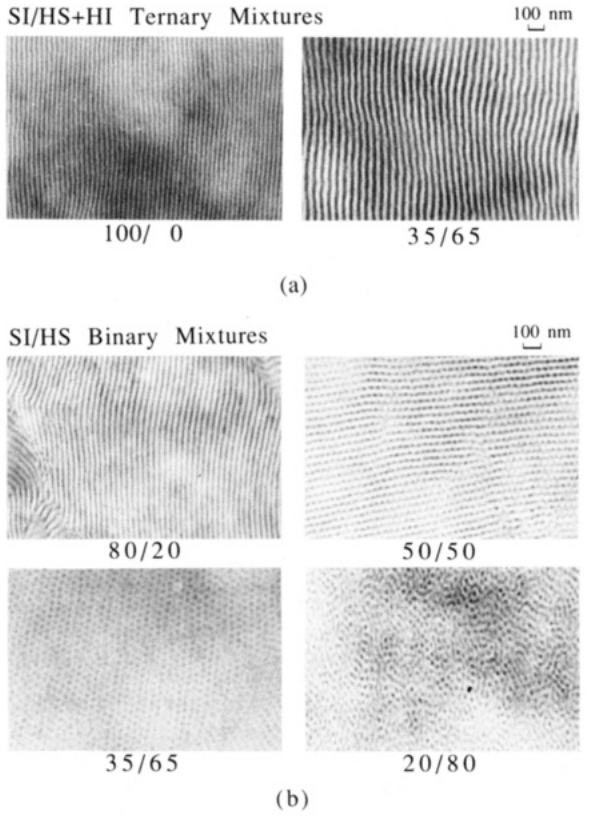

Figure 3. Transmission electron micrographs of the ultrathin sections of the film specimens stained by osmium tetraoxide: (a) pure SI and the ternary mixture and (b) the binary mixtures. The first three or two digits below each micrograph indicate the weight percent of SI in the mixture.

sections picked up on electron microscope grids coated with poly(vinyl formal) and carbon-supporting films were further stained by exposure to osmium tetraoxide vapor for a few hours. Electron microscopic observation was done with a Hitachi H-600 transmission electron microscope operated at 100 kV.

3. Small-Angle X-ray Scattering. The microdomain structures were investigated by small-angle X-ray scattering (SAXS) using a 12-kW rotating-anode X-ray generator operated at 50 kV and 200 mA, a 1.5-m SAXS camera with a graphite monochromator, and a one-dimensional position-sensitive proportional counter.[15] The SAXS profiles were corrected for the air scattering, the absorption, and the background scattering due to thermal diffuse scattering (TDS). The profiles were further corrected for the slit-height and slit-width smearing effects when necessary.[16] The slit-width and -height weighting functions for our SAXS optics were found to be given by Gaussian functions with standard deviations of $\sigma_W = 3.21 \times 10^{-3}$ nm^{-1} and $\sigma_H = 8.18 \times 10^{-4}$ nm^{-1}, respectively, in the unit of the reduced scattering angle s

$$s = (2 \sin \theta)/\lambda \qquad \text{(II.1)}$$

where 2θ and λ are the scattering angle and the wavelength (0.154 nm), respectively, of the incident X-ray beam. The absolute SAXS intensity was also measured by using the nickel foil method.[17] However, the absolute intensity itself is not of primary importance in this study.

III. Results

1. Transmission Electron Microscopy. Figure 3 shows typical transmission electron micrographs obtained for the ultrathin sections stained by osmium tetraoxide. The dark portions in the micrographs correspond to PI domains selectively stained by osmium tetraoxide. Figure 3a shows typical micrographs for pure SI block polymer (100/0) and the ternary mixture of 35/65 where the first three or two digits represent the weight percent of SI in the ternary mixtures. Pure SI and all the ternary mixtures of 80/20, 65/35, 50/50, 35/65, and 20/80 were found to exhibit the alternating lamellar microdomains with a long-range spatial order as typically shown in Figure 3a. Figure 3b shows typical micrographs for the binary mixtures of SI/HS 80/20, 50/50, 35/65, and 20/80. It was found that 80/20 exhibited the lamellar microdomains, 65/35 and 50/50 the cylindrical microdomains of PI in the matrix of PS, and 35/65 and 20/80 the spherical microdomains of PI in the matrix of PS, all the morphologies with a long-range spatial order.

All the micrographs exhibit only the microdomain structures but no domains where the homopolymers HS and/or HI segregated themselves as an independent phase. Hence, all the homopolymers were found to be incorporated into the microdomain space. This result was also confirmed with the ternary mixture with 10/90 composition.

2. Change of SAXS Profiles with Homopolymers. Figure 4 shows changes of SAXS profiles for binary mixtures where the first digits indicate the weight percent of SI in the mixture. The profile for pure SI shows higher order maxima at the peak positions, which are integer multiples of the first-order peak, suggesting the existence of the alternating lamellar microdomains with a long-range spatial order. With increasing HS content the lamellar microdomains are maintained as shown in Figure 4a. The relative peak heights of the higher order maxima change because of the increase in the volume fraction of PS lamellar microdomains relative to PI lamellae (see section III.3.A).

The lamellae are highly oriented with their interfaces parallel to the film surfaces as reported previously.[18,19] The film specimens were stacked parallel to each other. Their surfaces were set parallel to the slit-height direction of the line-focused X-ray image, and the SAXS profiles were obtained in the direction normal to the film surfaces with the position-sensitive proportional counter. Under this experimental condition the SAXS profiles are hardly smeared by the slit-height smearing effect.

Upon further increase of HS fraction, the SAXS profiles exhibit the multiple-order scattering maxima at peak positions of $1:(3)^{1/2}:(4)^{1/2}:(7)^{1/2}:(9)^{1/2}:\ldots$ relative to that of the first-order peak as shown in Figure 4b, implying the existence of the hexagonally packed cylindrical microdomains with a long-range spatial order. The volumetric considerations and the electron microscopic evidence shown in Figure 3 reveal that PI forms the cylindrical microdomains. The mixture of 65/35 shows even additional higher order peaks; one overlapped peak at $(12)^{1/2}$ and $(13)^{1/2}$ and the other at $(16)^{1/2}$ relative to the first-order peak. The peak located at $(3)^{1/2}$ for the 65/35 mixture and that located at $(4)^{1/2}$ for the 50/50 mixture are suppressed relative to the other peaks, which is due to the effect of the volume fraction of the cylinders on the scattering.[20]

The broad peaks marked with thick arrows labeled i = 1 and 2 indicate the first- and second-order peaks, respectively, from the isolated cylindrical microdomains located at $2\theta_{max,i}$

$$(4\pi/\lambda)R \sin \theta_{max,i} = 4.98, 8.364, 11.46, \ldots \qquad \text{(III.1)}$$

for $i = 1, 2, 3, \ldots$, respectively, where $2\theta_{max,i}$ is the scattering angle for the ith peak from the isolated cylinders and R is the average radius of the cylinders. The SAXS profiles were measured under the same configuration as those for the samples having lamellar morphology (Figure 4a). Again the cylindrical axes are highly oriented parallel to the film surfaces,[1] and hence the slit-height smearing effect on the

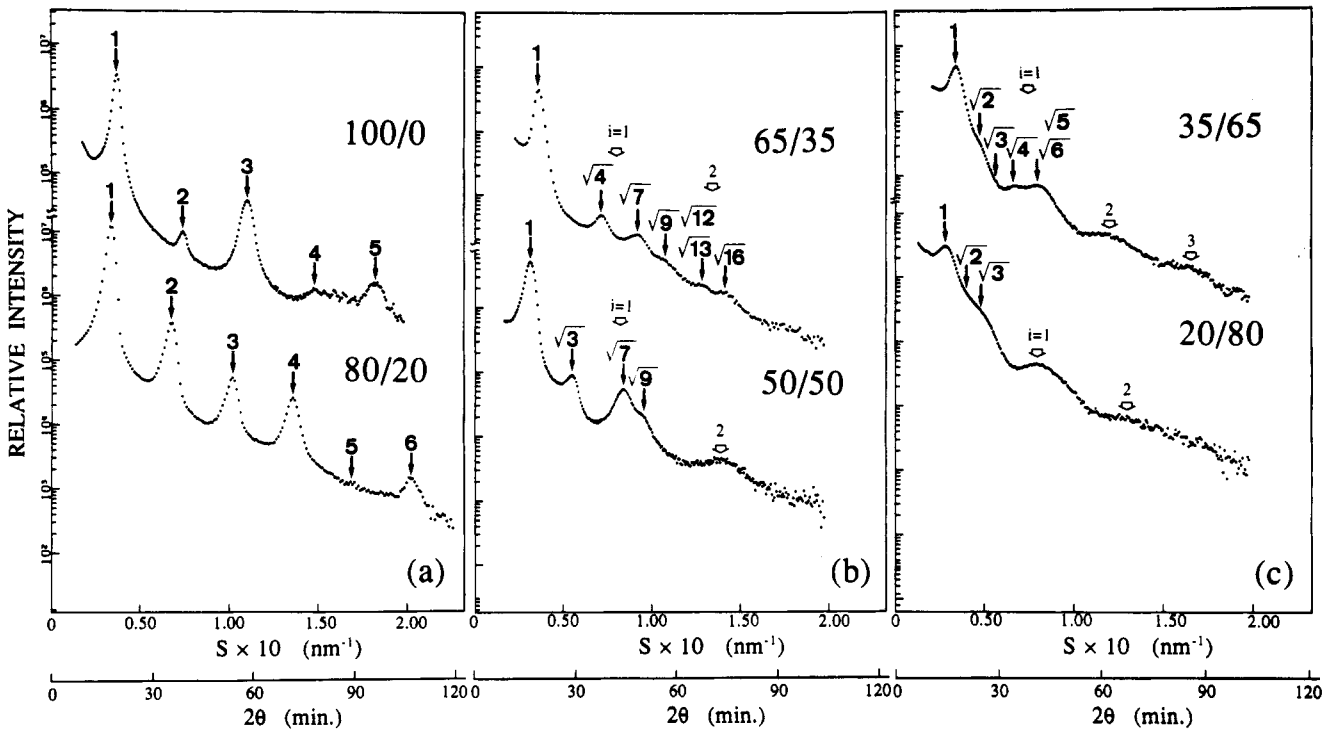

Figure 4. SAXS profiles from the binary mixtures with the composition of SI/HS (wt %/wt %) being (a) 100/0 and 80/20 (having the lamellar microdomains), (b) 65/35 and 50/50 (having the cylindrical microdomains), and (c) 35/65 and 20/80 (having the spherical microdomains).

SAXS profiles is not significant.

Upon further increase of HS the SAXS profiles change as shown in Figure 4c where they show the higher order maxima at the peak positions of $1:(2)^{1/2}:(3)^{1/2}:(4)^{1/2}:...$ relative to that of the first-order peak, implying the existence of the spherical microdomains with a long-range spatial order. The volumetric considerations and the electron mciroscopic observations as shown in Figure 3b indicate that PI forms the spheres. Furthermore, the volumetric considerations and the detailed SAXS analyses in section III.3 indicate that the spheres are arranged in space with a body-centered cubic symmetry. The thick arrows labeled i (i = 1–3) indicate the ith order maximum from the isolated spheres

$$(4\pi/\lambda)R \sin \theta_{\max,i} = 5.765, 9.10, 12.3, ... \quad \text{(III.2)}$$

for i = 1, 2, 3, ..., respectively, where R is the average radius of the spheres. Again the SAXS profiles shown in Figure 4c are the smeared profiles. Since the slit-height smearing effects on the profiles cannot be neglected for the spherical microdomains, the value R and intersphere distance D were estimated from the desmeared SAXS profiles.

From the SAXS profiles shown in Figure 4 one can determine the average interdomain distance D, i.e., the domain identity period for the lamellae and the nearest-neighbor distance between the microdomains for the cylinders and the spheres, and the average radius R_{PI} of PI cylinders (eq III.1) or spheres (eq III.2). The interdomain distance D can be determined from the corresponding Bragg spacings

$$D = d_{001} \quad \text{(III.3)}$$

for the lamellar microdomains

$$D = (4/3)^{1/2} d_{100} \quad \text{(III.4)}$$

for the hexagonally packed cylindrical microdomains

$$D = (3/2)^{1/2} d_{110} \quad \text{(III.5)}$$

for the spherical microdomains with the body-centered cubic symmetry. The Bragg spacing, in turn, is determined form the multiple-order diffraction maxima

$$2d_{00l} \sin \theta_{00l} = \lambda, \quad l = \text{integers} \quad \text{(III.6)}$$

$$d_{00l} = D/l \quad \text{(III.7)}$$

for the lamellar microdomains

$$2d_{hk0} \sin \theta_{hk0} = \lambda, \quad h, k = \text{integers} \quad \text{(III.8)}$$

where

$$d_{hk0} = D/[(4/3)(h^2 + hk + k^2)]^{1/2} \quad \text{(III.9)}$$

for the hexagonally packed cylindrical microdomains, and

$$2d_{hkl} \sin \theta_{hkl} = \lambda, \quad h, k, l = \text{integers} \quad \text{(III.10)}$$

where

$$d_{hkl} = D/[(3/4)(h^2 + k^2 + l^2)]^{1/2} \quad \text{(III.11)}$$

for the spherical microdomains with the body-centered cubic symmetry.

The values D and R_{PI} thus estimated directly from the SAXS profiles were summarized in the second and third columns in Table II. It is natural that D increases with increasing HS content, as is seen in Figure 4 by a systematic shift of the first-order peak position toward smaller s with increasing HS content. However, it is interesting to note that the value R for PI cylinders or that for PI spheres tends to decrease with increasing HS. The interpretation for this effect is not as obvious as that for D as a function of ϕ_b and will be given in section IV.

Figure 5 shows the SAXS profiles for the ternary mixtures. The ternary mixtures were prepared along the isopleth line so that overall weight fractions of styrene and isoprene segments are kept constant to 0.48 and 0.52, respectively, regardless of the weight fraction of SI block polymer. All the profiles show those relevant to the alternating lamellar microdomain, with its interdomain distance (or spacing, identity period) increasing with

Table II
Characterization of Microdomains for Binary Mixtures

specimens SI/HS	interdomain distance (D), nm	size of PI domain, nm		vol of PI domain		morphology
		$D_{PI,SAXS}$ or $R_{PI,SAXS}$, nm[a]	$D_{PI,vol}$ or $R_{PI,vol}$, nm[b]	SAXS	vol[b]	
100/0	27.1	14.2[c]	14.7[c]	0.53	0.55	lamella
80/20	30.0	12.4[c]	12.9[c]	0.41	0.44	lamella
65/35	33.2	10.0[d]	10.2[d]	0.33	0.34	cylinders[e]
50/50	35.6	9.5[d]	9.8[d]	0.26	0.27	cylinders[e]
35/65	36.2	12.2[f]	11.9[f]	0.21	0.19	spheres[g]
20/80	40.7	11.2[f]	11.1[f]	0.11	0.12	spheres[g]

[a] Determined from the best fit of experimental and theoretical SAXS profiles. [b] Determined from the volumetric considerations (see eqs IV.1–IV.3). [c] Thickness of PI lamellae. [d] Radius of PI cylinders. [e] Hexagonally packed cylinders. [f] Radius of PI spheres. [g] Body-centered cubic symmetry.

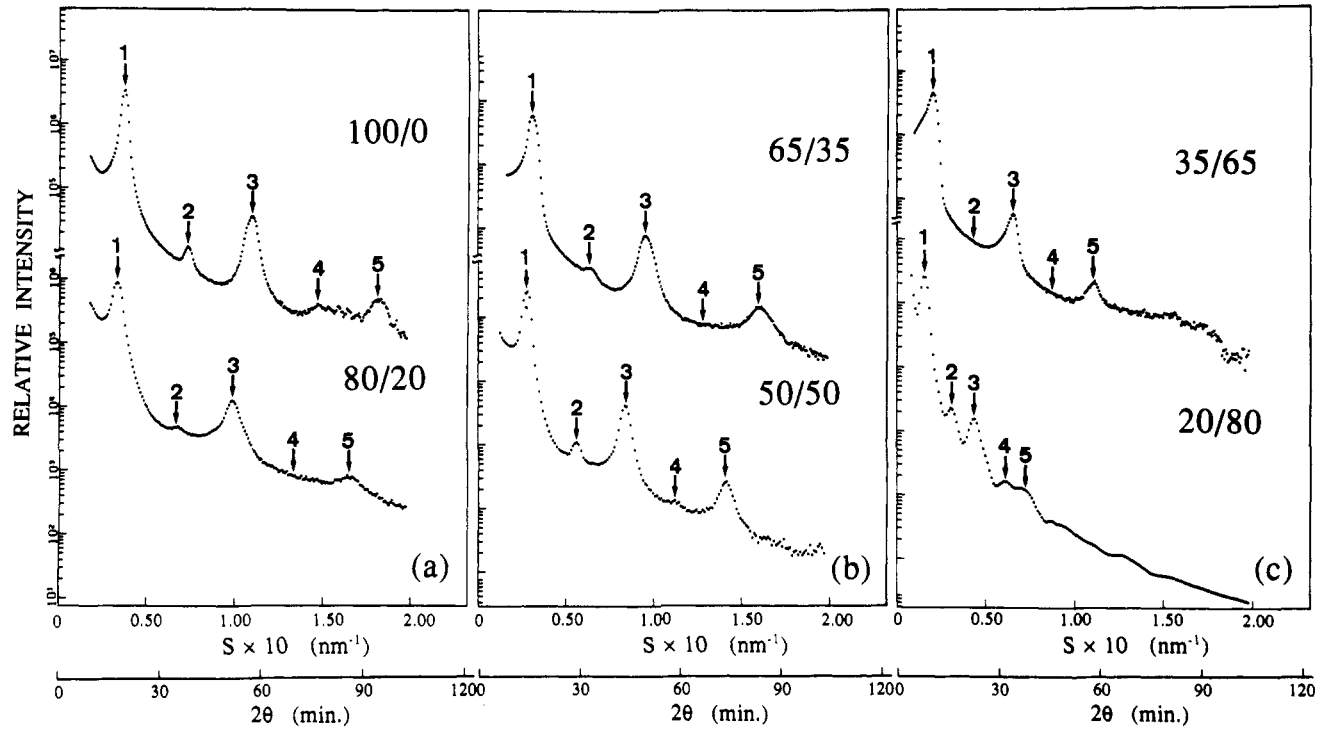

Figure 5. SAXS profiles from the ternary mixtures of SI/HS/HI with the weight percent of SI being (a) 100 and 80, (b) 65 and 50, and (c) 35 and 20. The mixtures were prepared only along the isopleth line so that the weight fractions of styrene and isoprene monomers were always kept constant, being equal to those of SI block polymer.

Table III
Characterization of Lamellar Microdomains for Ternary Mixtures

specimens	100/0	80/20	65/35	50/50	35/65	20/80
D_{SAXS},[a] nm	26.7[b]	28.6	31.0	34.4	46.3	65.3

[a] Interdomain distance obtained from SAXS (see eqs III.3, III.6, and III.7). [b] This value is a little different from the D value of the 100/0 specimen listed in Table II because the latter was obtained by the curve-fitting analysis.

increasing HS and HI contents, as seen in the systematic shift of each peak position toward smaller s. The results are summarized in Table III. Relative peak heights change slightly with the addition of HS and HI, implying that the relative volume of the two lamellar domains changes with the homopolymer addition. This effect may be primarily due to the asymmetry in bulk density between HS and HI.

3. Theoretical Analyses of SAXS Profiles. We present here the paracrystal analyses of the SAXS profiles for the lamellar and spherical microdomains with the corresponding long-range spatial orders. Evaluation of the volume fraction of one type of lamellae in the lamellar microdomain systems was qualitatively discussed by Skoulios.[21] As for the analyses on the lamellar microdomains, we aimed to analyze the thickness of each lamellar microdomain, i.e., D_{PI} and D_{PS} for the thicknesses of PI and PS lamellae, respectively, where $D = D_{PI} + D_{PS}$ and $\phi_{PS} = D_{PS}/D$, the volume fraction of PS lamellae. As for the analyses on the spherical microdomains, we aimed to analyze the symmetry of the cubic macrolattice.

A. Paracrystal Analyses of Lamellar Microdomains. Detailed formulation of the scattering equation for the one-dimensional paracrystals was presented elsewhere[22] in order to describe the SAXS scattering from the lamellar microdomains. The theoretical scattering profile based upon the paracrystal model was fitted to the experimental (desmeared) SAXS profiles measured with a point focused X-ray image for the highly oriented lamellar microdomains. The best fit enables us to extract various parameters characterizing the paracrystal model such as D, ϕ_{PS}, g, σ_{PS}, and t.[22] Here g is the paracrystal distortion factor defined by

$$g \equiv \sigma_D/D \qquad \text{(III.12)}$$

where σ_D is the standard deviation of the interlamellar distance from the average value D, σ_{PS} is the standard deviation on the thickness of PS lamella, and t is the characteristic interfacial thickness of the domain boundary region between PS and PI lamellae ($t = (2\pi)^{1/2}\sigma$ in refs 1

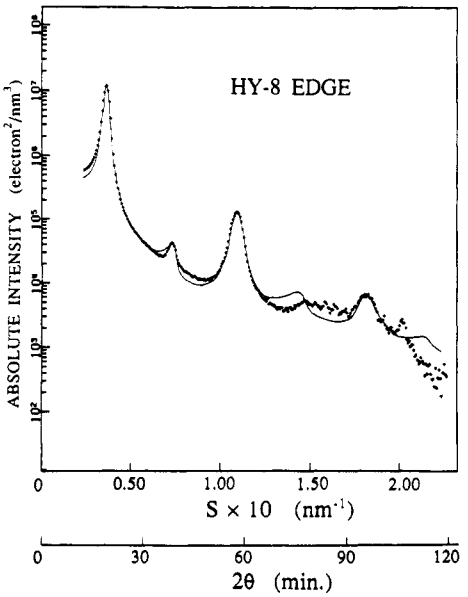

Figure 6. Best fit theoretical (solid line) and the experimental SAXS profile (profile shown by data points) for SI. The best fit was obtained for D = 27.1 nm, ϕ_{PS} = 0.47, g = 0.04, ϕ_{PS} = 0.6 nm, and t = 2.0 nm.

and 19). Here we employ a method of the best fit on the smeared profiles, viz., the smeared experimental SAXS profiles were best-fitted with the smeared theoretical profiles, the detailed methods of which will be described elsewhere.[23]

It should be emphasized here that a number of the fundamental parameters could be, more or less, uniquely determined, owing to the existence of a number of higher order peaks up to the sixth order and owing to the fact that each parameter affects the profile in sufficiently different manners; D affects the peak position, g affects the number of higher order diffraction maxima, ϕ_{PI} affects relative peak heights as will be demonstrated in Figure 7, σ_{PI} affects the damping of the higher order maxima, in a manner similar to the g factor but with σ_{PI} being more sensitive to the higher order peaks than g, and t affects q-dependence of the scattering profile at larger scattering angles. Upon increasing the value t, the scattering profile at the large angle tail tends to decay more rapidly with q.

Figure 6 shows the typical paracrystal analysis for the pure block polymer SI where the experimental profile and the best fit theoretical profile are shown by the dots and the solid line, respectively. The existence of a number of higher order scattering maxima allows one to determine unequivocally those parameters as described above, D = 27.1 nm, ϕ_{PS} = 0.47, g = 0.04, σ_{PS} = 0.6 nm, and t = 2.0 nm. It should be highlighted here that ϕ_{PS} obtained by the SAXS analyses agrees well with ϕ_{PS} = 0.45 calculated from the composition by elemental analysis, implying that PS and PI chains are almost completely segregated into their own microdomains. This is a phenomenon relevant to the strong segregation limit. It should be noted also that g is quite small, and hence the lamellar microdomains have the long-range order with only a small distortion.

Figure 7 shows how sensitively one can determine the volume fraction of one kind of lamellar microdomain. It is seen that a small change in the volume fraction of one type of lamellar microdomains ϕ (e.g., ϕ_{PS}) causes a big effect on the peak heights of the even-order diffractions. The best fit gives ϕ_{PS} = 0.47 ± 0.01, from which D_{PI} given

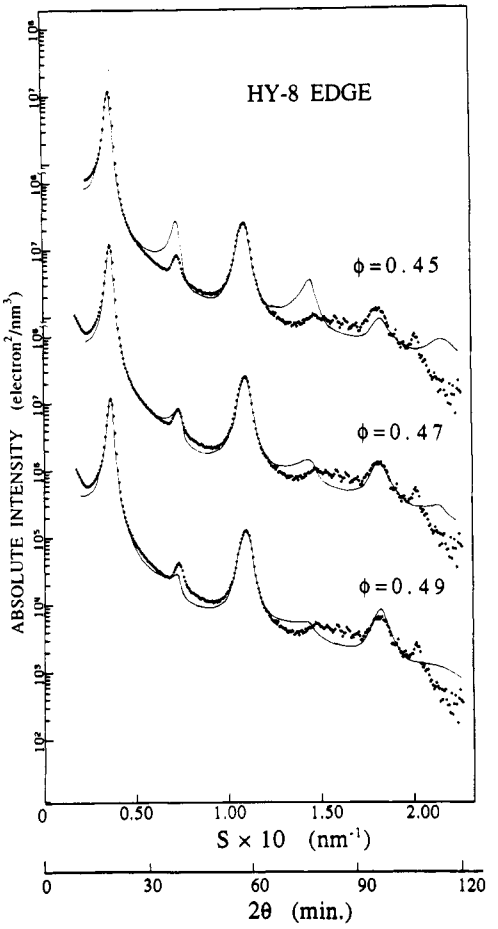

Figure 7. Effect of changing ϕ (the volume fraction of one type of the lamellar microdomains, e.g., ϕ_{PS} for PS lamellae) on the theoretical SAXS profiles. The solid lines are the theoretical profiles obtained for ϕ = 0.45, 0.47, and 0.49. The best fit was obtained for ϕ_{PS} = 0.47. Other parameters are the same as those in Figure 6.

in Table II was obtained

$$D_{PI} = (1 - \phi_{PS})D \qquad \text{(III.13)}$$

It should be noted that the scattering profile alone cannot uniquely determine whether the volume fraction refers to that of PI or PS lamellae, due to the reciprocity principle of scattering. However, one can unequivocally determine this from the volumetric consideration.

Figure 8 shows the similar paracrystal analysis for the SAXS profile from the lamellar microdomains observed for the binary mixture of SI/HS 80/20 (wt %/wt %). The best fit yielded the following results: D = 30.0 nm, g = 0.04, ϕ_{PS} = 0.59, σ_{PS} = 0.6 nm, and t = 2.7 nm. In the case when HS is completely solubilized into PS lamellae, ϕ_{PS} calculated from the volumetric consideration gives 0.58, in agreement with ϕ_{PS} determined by the paracrystal analysis of the SAXS profile. This implies again that HS is almost *completely solubilized* into PS lamellae. The values D and D_{PI} thus obtained are summarized in Table II. It should also be noted that the long-range order is not perturbed at all by HS, as g does not increase with HS.

B. Paracrystal Analysis of Spherical Microdomains. The scattering theory for the three-dimensional paracrystals for which the spherical microdomains are packed in space with a simple cubic (sc), a body-centered cubic (bcc), and a face-centered cubic lattice (fcc) was presented elsewhere[24] and hence will not be repeated here. The paracrystal analyses were performed on the desmeared SAXS profiles. Figure 9 shows the best fit SAXS

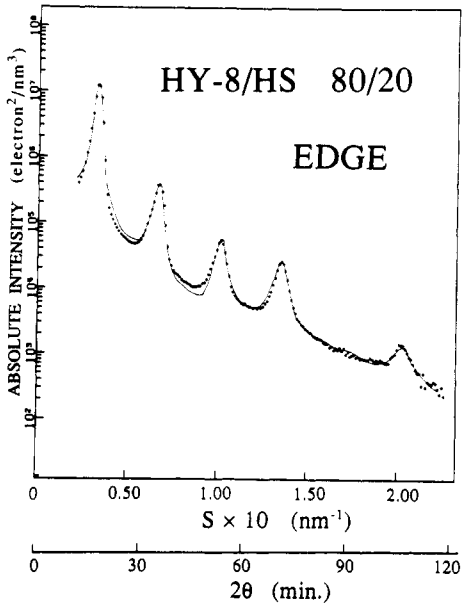

Figure 8. Best fit theoretical (solid line) and the experimental SAXS profile (profile shown by the data points) for a binary mixture of SI/HS 80/20 (wt %/wt %). The best fit was obtained for D = 29.3 nm, g = 0.04, ϕ_{PS} = 0.59, σ_{PS} = 0.6 nm, and t = 2.7 nm.

curves for (a) the binary mixture of SI/HS 35/65 and (b) SI/HS 20/80 where the experimental profiles were shown by the data points and the best fit theoretical profiles for sc, bcc, and fcc were shown by the corresponding solid lines.

Comparisons of the best fit theoretical curves for sc, bcc, and fcc with the experimental profiles clearly reveal that bcc symmetry gives the best results for the two mixtures. Fcc packing predicts the higher order maxima at the peak positions of $(4/3)^{1/2}$ and $(8/3)^{1/2}$ relative to the first-order peak as can be seen in the calculated curve (solid line). However, these higher order peaks were not identified in the experimental profile. Instead, a broad peak possibly comprised of the two overlapped peaks located at $(2)^{1/2}$ and $(3)^{1/2}$ relative to the first-order peak was identified. Thus bcc and sc packings are more reasonable than fcc packing. Bcc packing predicts the relative height of the first-order peak and the broad overlapped peak much better than sc packing does. The best fits yield bcc lattices with D = 36.2 nm, R = 12.2 nm, σ_R = 1.4 nm, g = 0.11, and t = 1.3 nm for SI/HS 35/65 (wt %/wt %) (a) and with D = 40.7 nm, R = 11.2 nm, σ_R = 1.3 nm, g = 0.14, and t = 0.4 nm for SI/HS 20/80 (wt %/wt %). The quantity σ_R is the standard deviation of R. The volume fractions of PI spheres (ϕ_{PI}) as calculated from D and R are 0.087, 0.113, and 0.123 for sc, bcc, and fcc, respectively. The volumetric considerations give ϕ_{PI} = 0.116 by assuming a complete segregation between PS and PI and a complete solubilization of HS into PS matrix. This value estimated by the volumetric considerations agrees most closely with ϕ_{PI} estimated from the SAXS analysis for bcc. Hence, the volumetric considerations also favor bcc symmetry.

IV. Discussion

1. Solubilization of Homopolymers into Microdomain Space. Here we quantitatively investigate the amount of the homopolymers solubilized into the microdomain space.

A. Binary Mixtures. If we assume that (i) HS is completely solubilized into PS microdomains and that (ii) PS and HS are completely segregated from PI (the strong

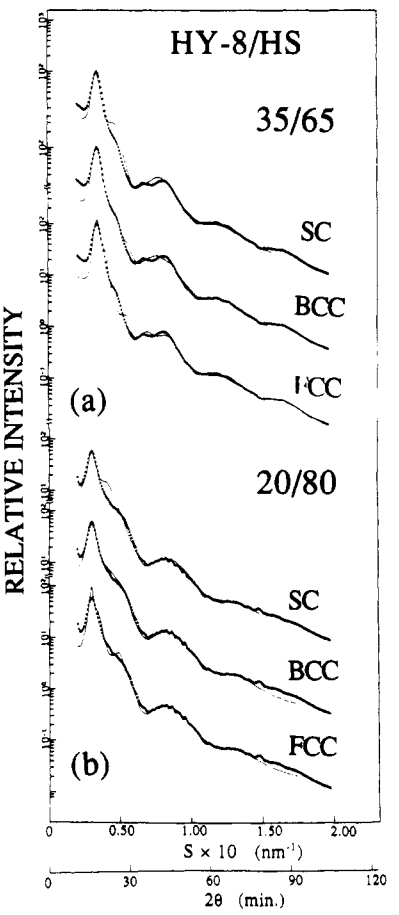

Figure 9. Best fit of the experimental SAXS profiles (the profiles shown by the data points) for binary mixtures of (a) SI/HS 35/65 (wt %/wt %) and (b) 20/80 (wt %/wt %) with the theoretical profiles (solid lines) obtained for the simple cubic (sc), the body-centered cubic (bcc), and the face-centered cubic (fcc) lattices. For each mixture bcc symmetry gives the best fit with the experimental result. The best fit for the mixture of SI/HS 35/65 (wt %/wt %) (a) was obtained for the bcc lattice with D = 36.2 nm, g = 0.11, R = 12.2 nm, σ_R = 1.4 nm, and t = 1.3 nm, and that for the mixture of SI/HS 20/80 (wt %/wt %) (b) was obtained for the bcc lattice with D = 40.7 nm, g = 0.14, R = 11.2 nm, σ_R = 1.3 nm, and t = 0.4 nm.

segregation limit), we can estimate the size of PI microdomains from the volumetric considerations. For the lamellar microdomains, the thickness of PI domains ($D_{PI,vol}$) can be calculated from the volumetric considerations

$$D_{PI,vol} = \phi_b(1-f)D \qquad \text{(IV.1)}$$

Similarly, for the cylindrical microdomains, the radius of PI cylinders hexagonally close-packed in space as shown in Figure 10a is given by

$$R_{PI,vol} = D\left[\frac{\sqrt{3}(1-f)\phi_b}{2\pi}\right]^{1/2} \qquad \text{(IV.2)}$$

and the radius of PI spheres in the bcc lattice as shown in Figure 10b is given by

$$R_{PI,vol} = D\left[\frac{(1-f)\phi_b}{\sqrt{3}\pi}\right]^{1/3} \qquad \text{(IV.3)}$$

These values were determined from D values measured by SAXS (the second column of Table II), ϕ_b, and f known for the given mixtures. The estimated values of $D_{PI,vol}$ and $R_{PI,vol}$ are summarized in the fourth column in Table II. The estimated values $D_{PI,vol}$ agree almost perfectly with the corresponding values $D_{PI,SAXS}$ and $R_{PI,SAXS}$ determined by SAXS (listed in the third column of Table II), indicating

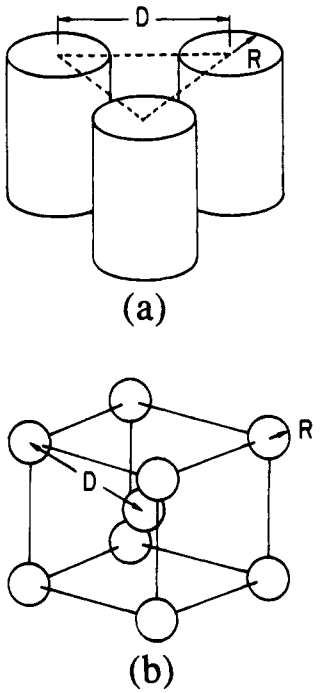

Figure 10. Hexagonally close-packed cylindrical microdomains (a) and spherical microdomains with a body-centered cubic lattice (b) and the definitions of D and R.

that HS's are all solubilized somewhere in the PS microdomain space.

B. Ternary Mixtures. For the ternary mixtures the lamellar thicknesses of PS and PI lamellae, D_{PI} and D_{PS}, respectively, depend on a_J as well as the amount of the homopolymers selectively solubilized

$$D_{PI} = D_{PI}(a_J,\phi_{HIS}) \tag{IV.4a}$$

and

$$D_{PS} = D_{PS}(a_J,\phi_{HSS}) \tag{IV.4b}$$

Here ϕ_{HIS} and ϕ_{HSS} are the amount of HI and HS solubilized into PI and PS microdomains, respectively. Thus there are three unknown quantities, a_J, ϕ_{HIS}, and ϕ_{HSS}, and two measurable quantities, D_{PI} and D_{PS}, using SAXS. Thus ϕ_{HIS} and ϕ_{HSS} cannot be uniquely determined on the contrary to the case of the binary mixtures. Obviously ϕ_{HSS} can be uniquely determined for the binary mixtures with $\phi_{HIS} = 0$, which is the basis of the analysis given in section IV.1.A.

2. Swelling of Microdomains by Homopolymers. Here we further advance our analyses on the swelling behavior of the homopolymers and investigate whether the swelling involves the localized or uniform solubilization of the homopolymers (see parts b and c of Figure 1). It is intuitively obvious from the consideration related to Figure 1 that the difference in the swelling or solubilization behavior causes the difference in the expansion of the interdomain distance with the homopolymer content.

Figure 11 shows the expansion of the interdomain distance relative to D_0, the interdomain distance for pure SI, as a function of the block polymer volume fraction ϕ_b in the ternary (solid circles) and binary mixtures (open circles). The solid lines were obtained with the least-squares fits with polynomials.

$$D/D_0 = 1.0 + 0.6\phi_H \tag{IV.5}$$

for the binary mixtures, and

$$D/D_0 = 1.0 + 0.1884\phi_H - 0.1966\phi_H^2 + 2.5219\phi_H^3 \tag{IV.6}$$

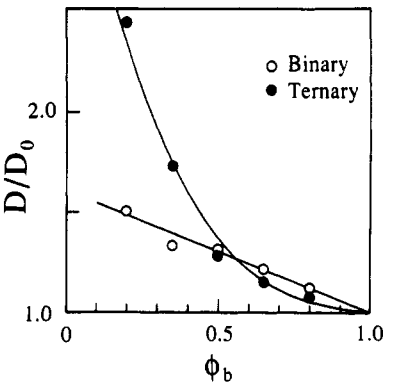

Figure 11. Expansion of the interdomain distance upon addition of HS and/or HI as a function of the volume fraction of SI in the ternary (filled circles) and the binary mixtures (open circles). The lines show the least-squares fits with polynomials: (a) $D/D_0 = 1.0 + 0.1884\phi_H - 0.1966\phi_H^2 + 2.5219\phi_H^3$ for the ternary mixture and (b) $D/D_0 = 1.0 + 0.6\phi_H$ for the binary mixtures, $\phi_H = 1 - \phi_b$.

for the ternary mixtures, where ϕ_H (=1 − ϕ_b) is the volume fraction of the homopolymers in the mixtures.

From the volumetric considerations we can interrelate this expansion D/D_0 with the change of the interfacial density of the chemical junctions ρ_J/ρ_{J0}, which is intimately related to the swelling or solubilization behavior. Here ρ_J and ρ_{J0} are the interfacial densities of the chemical junctions of the block polymers after and before the homopolymer addition.

$$\frac{D}{D_0} = \frac{\rho_J}{\rho_{J0}\phi_b} \tag{IV.7}$$

for the alternating lamellar microdomains

$$\frac{D}{D_0} = \frac{\rho_J}{\rho_{J0}}\left[\frac{2\sqrt{3}\pi(1-f)}{3\phi_b}\right]^{1/2} \tag{IV.8}$$

for the hexagonally packed cylindrical microdomains of PI, and

$$\frac{D}{D_0} = \frac{\rho_J}{\rho_{J0}}\left[\frac{27\sqrt{3}\pi(1-f)^2}{8\phi_b}\right]^{1/3} \tag{IV.9}$$

for the spherical microdomains with bcc packing. The localized solubilization of the homopolymers as an extreme gives $\rho_J/\rho_{J0} = 1$, which gives D/D_0 as a function of ϕ_b, as shown in Figure 12, for the lamellar (solid line), cylindrical (dash-dot line), and spherical microdomains (broken line). It predicts the expansion D/D_0 much larger than the real expansion, implying that the solubilization of the homopolymers is more uniform than the localized solubilization model. It should also be noted that the value D_0 in eqs IV.8 and IV.9 is the one for the lamellar microdomain for the pure diblock copolymer. Equation IV.7 is applied to both the binary and ternary mixtures, but eqs IV.8 and IV.9 are applied only to the binary mixtures.

From the measured value of D/D_0 and ϕ_b and f, which are known for a given mixture, one can calculate the expansion a_J/a_{J0} where a_J and a_{J0} are the average nearest-neighbor distances between the chemical junctions after and before the addition of the homopolymers

$$\frac{a_J}{a_{J0}} \equiv \left(\frac{\rho_J}{\rho_{J0}}\right)^{-1/2} \tag{IV.10}$$

The results are shown in Figure 13 as a function of ϕ_b for the binary (open circles) and ternary mixtures (solid circles). It is spectacular to note that the results on the binary and ternary mixtures became nearly identical when

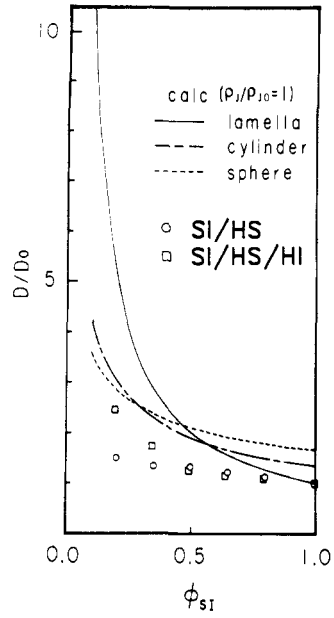

Figure 12. Comparisons between the theoretical and the experimental results on D/D_0 as a function of ϕ_b. The experimental results for the binary and the ternary mixtures are shown by circles and squares, respectively. The theoretical results are calculated for the "localized solubilization" (i.e., $\rho_J/\rho_{J0} = 1$) for the lamellar (solid line), the cylindrical (dash-dot line), and the spherical microdomains (broken line).

a_J/a_{J0} was plotted as a function of ϕ_b. The solid line indicates the least-squares fit of the experimental results with the polynomial

$$a_J/a_{J0} = 1.0 + 0.2914\phi_H + 0.2843\phi_H^2 \quad \text{(IV.11)}$$

Obviously a substantial amount of the lateral swelling was found to be induced by the homopolymer solubilization.

3. Qualitative Predictions on Solubilization of Homopolymers. Here we shall attempt to qualitatively analyze the experimental results shown in Figures 11 and 13 on the swelling of the microdomains by the homopolymers or the solubilization of the homopolymers into the microdomain space. Quantitative theoretical analyses of the experimental results are beyond the scope of the present paper and deserve future studies.

For simplicity we treat here the ternary mixtures of A–B + A + B, where we have only the lamellar microdomains regardless of ϕ_b. Consider the free energy per chain, F_{chain}, for the alternating lamellar microdomains of A and B lamellae with thicknesses D_A and D_B, respectively

$$\frac{F_{chain}}{k_BT} = \gamma_0\Sigma + \frac{3}{2}\left(\frac{D_A^2}{N_Ab^2} + \frac{D_B^2}{N_Bb^2}\right) + \frac{N_B}{2}\left[\frac{1-\phi_B}{N_B}\ln(1-\phi_B) + \frac{\phi_B}{P_B}\ln\phi_B\right] + \frac{N_A}{2}\left[\frac{1-\phi_A}{N_A}\ln(1-\phi_A) + \frac{\phi_A}{P_A}\ln\phi_A\right] \quad \text{(IV.12)}$$

where N_A and N_B are the degrees of polymerization (DP) of A and B block chains in an A–B diblock polymer, b is the Kuhn statistical segment length for the block chain, and k_B is Boltzmann's constant. P_A and P_B are the DP's for the homopolymers A and B uniformly solubilized into A and B lamellar domains, respectively. ϕ_A and ϕ_B are the volume fractions of A and B homopolymers in A and B lamellar microdomains, respectively. We assume here that A and B homopolymers are selectively solubilized into A and B lamellar microdomains, respectively. Σ is the interfacial area occupied by a single block chain, and γ_0 is the parameter associated with the interaction energy between A and B at the interface.

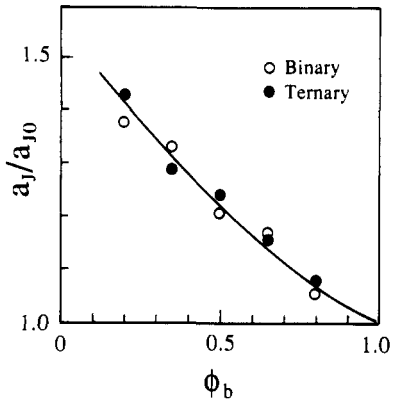

Figure 13. Lateral swelling of the microdomains by addition of the homopolymers as observed by the expansion of the average nearest-neighbor distance between the chemical junctions a_J/a_{J0}. The data for the binary and the ternary mixtures are shown by open and filled circles, respectively. The solid line shows the result of the least-squares fit with polynomials; $a_J/a_{J0} = 1.0 + 0.2914\phi_H + 0.2843\phi_H^2$, $\phi_H = 1 - \phi_b$. The same equation is applied for both the binary and the ternary mixtures.

The first term in the right-hand side of eq IV.12 is the interfacial energy; the second term is the conformational (stretching) free energy of the block chains, and the third and fourth terms are the mixing free energy. It should be noted here that, for quantitative analyses of the swelling behavior, the more rigorous expression should be used for the second term in the right-hand side of eq IV.12 in order to incorporate the features[3,25,26] unique to the confined chains that satisfy the demands of the spatial confinements of A and B chains in the respective domains, the uniform spatial segmental density profiles, and the incompressibility. The third and fourth terms on the right-hand side of eq IV.12 are constant, independent of D_A, D_B, and Σ, and hence insignificant in our arguments. The incompressibility gives the relationships

$$N_Bb^3 = D_B\Sigma(1-\phi_B) \quad \text{(IV.13)}$$

and

$$N_Ab^3 = D_A\Sigma(1-\phi_A) \quad \text{(IV.14)}$$

Equation IV.12 can be rewritten as a function of Σ by using eqs IV.13 and IV.14

$$\frac{F_{chain}}{k_BT} = \gamma_0\Sigma + \frac{3a^4}{2}\left[\frac{N_A}{(1-\phi_A)^2} + \frac{N_B}{(1-\phi_B)^2}\right]\Sigma^{-2} + C \quad \text{(IV.15)}$$

where C is a constant independent of Σ. The equilibrium value of Σ (Σ_{min}) can be obtained by minimizing F_{chain} with Σ

$$\partial(F_{chain}/k_BT)/\partial\Sigma = 0 \quad \text{(IV.16)}$$

Equation IV.16 gives

$$\Sigma_{min} = \left\{\frac{3a^4}{\gamma_0}\left[\frac{N_A}{(1-\phi_A)^2} + \frac{N_B}{(1-\phi_B)^2}\right]\right\}^{1/3} \quad \text{(IV.17)}$$

Σ_{min} for pure block polymer designated as Σ_0 is obtained by setting $\phi_A = \phi_B = 0$; i.e.

$$\Sigma_0 = \left[\frac{3a^4(N_A + N_B)}{\gamma_0}\right]^{1/3} \quad \text{(IV.18)}$$

Thus

$$\frac{a_J}{a_{J0}} = \left(\frac{\Sigma_{min}}{\Sigma_0}\right)^{1/2} = \left[\frac{f_A}{(1-\phi_A)^2} + \frac{f_B}{(1-\phi_B)^2}\right]^{1/6} \quad \text{(IV.19)}$$

Equation IV.17 is a general expression for the ternary system.

The equilibrium domain identity period $D = D_A + D_B$ for the ternary mixture can also be calculated from eqs IV.13, IV.14 and IV.17

$$D = \frac{b^3}{\Sigma_0}\left(\frac{N_A}{1-\phi_A} + \frac{N_B}{1-\phi_B}\right)\left[\frac{f_A}{(1-\phi_A)^2} + \frac{f_B}{(1-\phi_B)^2}\right]^{-1/3} \quad \text{(IV.20)}$$

D for the pure block polymer (D_0) can be obtained by setting $\phi_A = \phi_B = 0$ in eq IV.20

$$D_0 = (b^3/\Sigma_0)(N_A + N_B) \sim (N_A + N_B)^{2/3} \quad \text{(IV.21)}$$

Thus we obtain the $^2/_3$ power law,[1,19,27] and

$$\frac{D}{D_0} = \left(\frac{f_A}{1-\phi_A} + \frac{f_B}{1-\phi_B}\right)\left[\frac{f_A}{(1-\phi_A)^2} + \frac{f_B}{(1-\phi_B)^2}\right]^{-1/3} \quad \text{(IV.22)}$$

from eqs IV.20 and IV.21.

For the symmetric block polymer with $f_A = f_B = {}^1/_2$ and the ternary mixtures along the isopleth line, as in our experimental situations

$$\phi_A = \phi_B = 1 - \phi_b \quad \text{(IV.23)}$$

where ϕ_b is the volume fraction of A–B block polymer in the ternary mixtures. We obtain

$$a_J/a_{J0} = D/D_0 = \phi_b^{-1/3} \quad \text{(IV.24)}$$

It should be noted that we can calculate a_J/a_{J0} and D/D_0 also for the binary mixtures of A–B + B by setting $\phi_A = 0$ and finding the relationship between ϕ_b, the volume fraction of A–B block polymer in the binary mixtures, and ϕ_B

$$1 - \phi_B = \frac{\phi_b}{2 - \phi_b} \quad \text{(IV.25)}$$

as long as the mixtures have the lamellar microdomains.

Figure 14 compares the theoretical predictions for a_J/a_{J0} and D/D_0 given by eq IV.24 (solid line) with the experimental results for the ternary mixtures where the results for D/D_0 are shown by open circles and those for a_J/a_{J0} by filled circles. The predicted results nicely explain the general tendency observed in the experimental results. Especially, a fine agreement was obtained at a high copolymer content ϕ_b. With decreasing ϕ_b, i.e., with increasing the homopolymer content, discrepancies between the predicted and the experimental results appear to be remarkable in that (i) the experimental lateral swelling a_J/a_{J0} (filled circles) is less than that of the predicted a_J/a_{J0} (solid line) and (ii) the experimental longitudinal swelling D/D_0 (open circles) is higher than that of the predicted D/D_0 (solid line). The discrepancies (i) and (ii) are mutually interrelated and imply a tendency toward the localized solubilization of homopolymers A and B in the middle of the corresponding lamellar microdomains with increasing the homopolymer content.[31]

It is strongly desired to predict these experimental results more quantitatively based upon the theory,[9] which can deal with the spatial confinements of A and B block and homopolymer chains in the respective domains, while

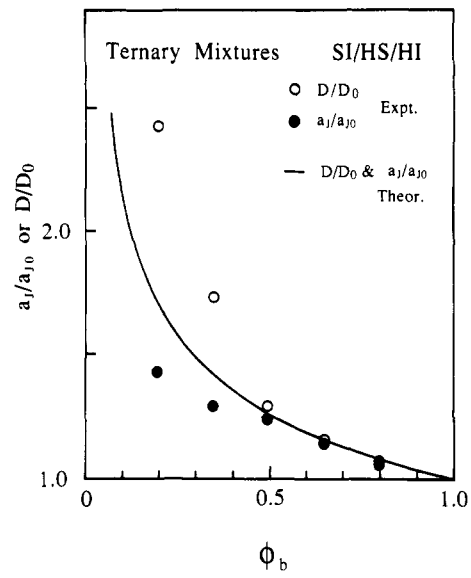

Figure 14. Comparisons between the predicted and the experimental results on a_J/a_{J0} and D/D_0 for the ternary mixtures of SI/HS/HI along the isopleth line. The experimental results for a_J/a_{J0} and D/D_0 shown by filled and open circles and the predicted results for a_J/a_{J0} and D/D_0 are identical and shown by the solid line.

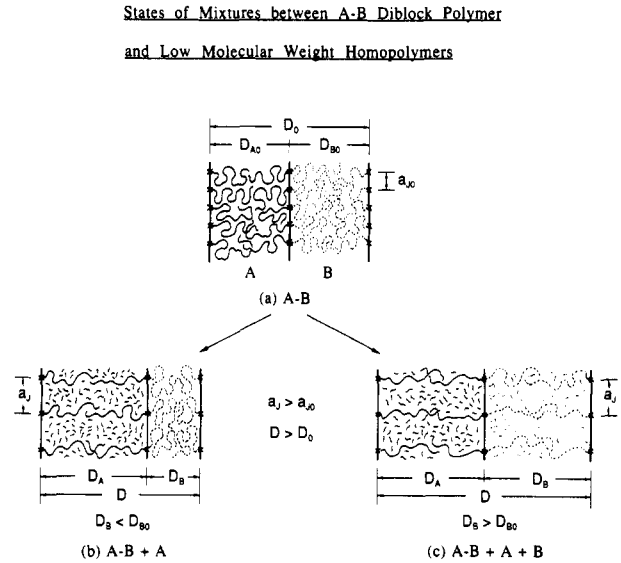

Figure 15. Sketches showing, more or less, the uniform solubilization of the homopolymer into the corresponding microdomains: (a) microdomains for the pure SI block polymer, (b) those for the binary mixtures of SI/HS, and (c) those for the ternary mixtures of SI/HS/HI.

maintaining the demands of the uniform spatial segmental density profiles for A + B segments. The theory is desired to predict the spatial segmental density profile for A and B block chains as well as for A and B homopolymer chains for the lamellar, cylindrical, and spherical microdomains.

V. Conclusions

1. Possible Solubilization Model. The low molecular weight homopolymers were found to be solubilized, more or less, uniformly into the corresponding microdomain space. As sketched in Figure 15b for the binary mixtures, the low molecular weight homopolymer A is solubilized into A microdomain, which generally causes the changes of the molecular conformations of A homopolymer chains and A block chains, both tending to the stretched normal to the lamellar interfaces.[29] The swelling causes the expansion of the average nearest-neighbor distance between

the chemical junctions from a_{J0} for the pure block polymer (Figure 15a) to a_J, which would then cause the contraction of the conformation of B block chains and hence the contraction of the thickness of B lamellae from D_{B0} to D_B in order to maintain the bulk density of B microdomains equal to that of pure B homopolymers. The decrease of D_B by the swelling is outweighed by the increase of D_A, resulting in the increase of the identity period from D_0 to D upon swelling by A homopolymers.

Upon an increase in the content of the homopolymer A (ϕ_H), the conformational entropy loss due to the chain perturbation increases. This penalty of the conformational entropy loss is reduced by producing the curvature in the interface in such a way that the minority phase B forms the discrete microdomains of cylinders or spheres. This reduction of the penalty associated with the conformational entropy is accompanied by an increase of the penalty due to the curvature free energy. As ϕ_H increases, the free-energy penalty due to the conformational entropy becomes larger than that due to the curvature free energy, which would then causes the morphological transitions as discussed in this paper.

As sketched in Figure 15c for the ternary mixtures, the low molecular weight homopolymers A and B tend to be more or less uniformly solubilized into A and B lamellar microdomains, respectively. The solubilization causes the expansions of D_{A0}, D_{B0}, and a_{J0} to D_A, D_B, and a_J, respectively, as well as the expansions of the chain conformations of A and B block chains and A and B homopolymer chains in the direction normal to the interface. The free-energy penalty caused by the conformational entropy loss may be overcome by the free-energy gain due to the entropy increase associated with the placement entropy of the homopolymers. Since A and B microdomains are symmetric, the ternary mixtures keep the lamellar microdomains irrespective of ϕ_H.

It should also be highlighted that the microdomains and their long-range order are conserved down to a very low level of ϕ_b. The small amount of the block polymer ϕ_b, greater than the lowest $\phi_b = 0.1$ covered in this experiment, is sufficient to solubilize the homopolymers in the microdomains with the long-range order and to avoid the macroscopic phase separation of the homopolymers into the independent phase or phases. The critical ϕ_b ($\phi_{b,c}$) may be even lower than 0.1 covered in this experiment.

2. Qualitative Estimation of $\phi_{b,c}$. A qualitative estimation of $\phi_{b,c}$, the critical volume fraction of the block polymer below which the macroscopic phase transition occurs to result in the coexistence of the microdomain phase and the homopolymer phase, can be done by means of the thermodynamic stability analyses previously reported.[8]

Figure 16 shows the thermodynamic stability analyses for the binary mixtures (a) and the ternary mixtures (b) where the spinodal points for the macrophase transition $(\chi N_1)_{s,macro}$ (solid line) and for the microphase transition $(\chi N_1)_{s,micro}$ (broken line) are plotted as a function of ϕ_b. Here N_1 is the degree of polymerization of SI, and N_2 and N_3 are those of HS and HI, the weight-average polymerization indices being taken here. For the binary mixtures we obtain $N_2/N_1 = 0.067$, and for the ternary mixtures we obtain $N_2/N_1 = 0.067$ and $N_3/N_1 = 0.123$ from Table I. The values of $\phi_{b,c}$'s thus estimated are 0.04 and 0.08 for the binary and the ternary mixtures, which qualitatively account for the experimental $\phi_{b,c} < 0.2$

It should be noted that the value of $(\chi N_1)_{s,micro}$ increases with increasing the volume fraction of the homopolymers for both binary and ternary mixtures in Figure 16.

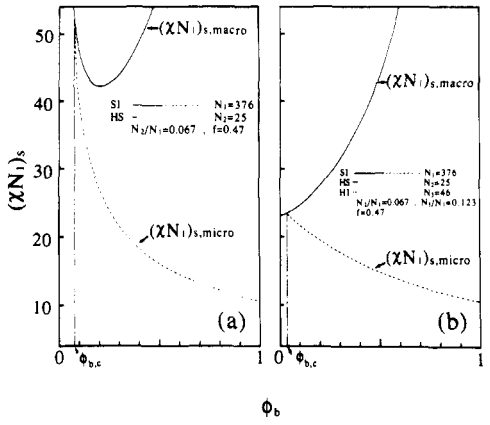

Figure 16. Phase diagrams for the spinodal points $(\chi N_1)_s$ for the macrophase transition $(\chi N_1)_{s,macro}$ (solid lines) and for the microphase transition $(\chi N_1)_{s,micro}$ (broken lines) plotted as a function of ϕ_b. $\phi_{b,c}$ is the critical volume fraction of the block polymer, above which the microphase transition can occur. N_1, N_2, and N_3 are the polymerization indices of SI, HS, and HI, respectively: (a) a binary mixture of SI/HS and (b) a ternary mixture of SI/HS/HI. In the ternary mixture the volume fractions of HS and HI are kept equal to f and $1 - f$, respectively.

This implies that the addition of the homopolymers, the molecular weight of which is considerably smaller than that of the corresponding block chains, decreases the spinodal temperature for the microphase transition. As the molecular weight of the homopolymers relative to that of the corresponding block chains increases, the opposite effect shows up, i.e., the addition of the homopolymers raises the microphase-transition temperature, which was experimentally observed by Cohen et al.[28] These effects of molecular weight can be easily predicted by theoretical calculations and have already been reported elsewhere.[8,9]

Acknowledgment. We gratefully acknowledge Dr. L. Leibler for suggesting the theoretical analyses discussed in section IV.3. We are also grateful to Dr. M. Whitmore and Dr. J. Noolandi for useful discussions. This work was supported in part by a Grant-in-Aid for Scientific Research 63470090 from the Ministry of Education, Science and Culture, Japan, by a research grant from the Mitsubishi Kasei Corp., and by a scientific grant from the Mitsubishi Foundation.

References and Notes

(1) See for example: Hashimoto, T.; Shibayama, M.; Fujimura, M.; Kawai, H. In *Block Copolymers—Science and Technology*; Meier, D. J., Ed.; Harwood Academic Publishers: London, New York, 1983; pp 63–108.
(2) See for example: Hashimoto, T. In *Thermoplastic Elastomers*; Legge, N. R., Holden, G., Schroeder, H. E., Eds.; Hanser: Munich, Vienna, New York, 1987; Chapter 12.
(3) Meier, D. J. Reference 2, Chapter 11.
(4) Thomas, E. L.; Alward, D. B.; Kinning, D. J.; Martin, D. C.; Handlin, D. J., Jr.; Fetters, L. J. *Macromolecules* **1986**, *19*, 2197.
(5) Hasegawa, H.; Tanaka, H.; Yamasaki, K.; Hashimoto, T. *Macromolecules* **1987**, *20*, 1651.
(6) Hong, K. M.; Noolandi, J. *Macromolecules* **1981**, *14*, 727.
(7) Inoue, T.; Soen, T.; Hashimoto, T.; Kawai, H. *Macromolecules* **1970**, *3*, 87.
(8) Tanaka, H.; Hashimoto, T. *Polym. Commun.* **1988**, *29*, 212; Hashimoto, T.; Tanaka, H.; Hasegawa, H. In *Molecular Conformation and Dynamics of Macromolecules in Condensed Systems*; Nagasawa, M., Ed.; Elsevier: Amsterdam, 1988; p 257.
(9) Hong, K. M.; Noolandi, J. *Macromolecules* **1983**, *16*, 1083; Whitmore, M. D.; Noolandi, J. *Macromolecules* **1985**, *18*, 2486.
(10) Zin, W.-C.; Roe, R.-J. *Macromolecules* **1984**, *17*, 189.
(11) Quan, X.; Gangarz, I.; Koberstein, J. T. *J. Polym. Sci., Part B: Polym. Phys.* **1987**, *25*, 641.

(12) Part 2 of this series: Hashimoto, T.; Tanaka, H.; Hasegawa, H. *Macromolecules* **1990**, *23*, 4378.
(13) Kinning, D. J.; Winey, K. I.; Thomas, E. L. *Macromolecules* **1988**, *21*, 3502.
(14) Hashimoto, T.; Nakamura, N.; Shibayama, M.; Izumi, A.; Kawai, H. *J. Macromol. Sci., Phys.* **1980**, *B17*, 389.
(15) Hashimoto, T.; Suehiro, S.; Shibayama, M.; Saijo, K.; Kawai, H. *Polym. J.* **1981**, *13*, 501.
(16) Fujimura, M.; Hashimoto, T.; Kawai, H. *Mem. Fac. Eng., Kyoto Univ.* **1981**, *43*, 224.
(17) Hendricks, R. W. *J. Appl. Cryst.* **1972**, *5*, 315.
(18) Hashimoto, T.; Nagatoshi, K.; Todo, A.; Hasegawa, H.; Kawai, H. *Macromolecules* **1974**, *7*, 314.
(19) Hashimoto, T.; Shibayama, M.; Kawai, H. *Macromolecules* **1980**, *13*, 1237.
(20) Hashimoto, T.; Harada, M.; Tanaka, H., to be submitted for publication.
(21) Skoulios, A. In *Block and Graft Copolymers*; Burke, J. J., Weiss, V., Eds.; Syracuse University Press: Syracuse, NY, 1973, p 121.
(22) Shibayama, M.; Hashimoto, T. *Macromolecules* **1986**, *19*, 740.
(23) Shibayama, M.; Hashimoto, T., to be submitted for publication.
(24) Matsuoka, H.; Tanaka, T.; Hashimoto, T.; Ise, N. *Phys. Rev. B* **1987**, *36*, 1754. Matsuoka, H.; Tanaka, H.; Iizuka, N.; Hashimoto, T.; Ise, N. *Phys. Rev. B* **1990**, *41*, 3854.
(25) Helfand, E. *Macromolecules* **1975**, *8*, 552. Helfand, E.; Wasserman, Z. R. *Macromolecules* **1976**, *9*, 879.
(26) Hashimoto, T.; Shibayama, M.; Kawai, H.; Meier, D. J. *Macromolecules* **1985**, *18*, 1855.
(27) Hashimoto, T.; Fujimura, M.; Kawai, H. *Macromolecules* **1980**, *13*, 1660. Shibayama, M.; Hashimoto, T.; Kawai, H. *Macromolecules* **1983**, *16*, 1434.
(28) Cohen, R. E.; Torradas, J. M. *Macromolecules* **1984**, *17*, 1101.
(29) Hasegawa, H.; Tanaka, T.; Hashimoto, T.; Han, C. C. *J. Appl. Crystallogr.*, in press.
(30) Berney, C. V.; Cheng, P.-L.; Cohen, R. E. *Macromolecules* **1988**, *21*, 2235.
(31) This tendency was also observed by Berney et al.[30] for the spherical microdomain systems composed of poly(styrene-*b*-butadiene) and deuteriated polystyrene homopolymer.

Registry No. SI (block copolymer), 105729-79-1; HS (homopolymer), 9003-53-6; HI (homopolymer), 9003-31-0.